Available online at www.sciencedirect.com
ScienceDirect
Earth and Planetary Science Letters 255 (2007) 148 – 163
EPSL
www.elsevier.com/locate/epsl

Two scales of inflation at Lastarria-Cordon del Azufre volcanic complex, central Andes, revealed from ASAR-ENVISAT interferometric data

J.-L. Froger [a,b,*], D. Remy [c,d], S. Bonvalot [c,d], D. Legrand [d]

[a] *Institut de Recherche pour le Développement (IRD)-UR163-UMR6524 (LMV)-UBP-CNRS-IRD, Obs. de Physique du Globe de Clermont-Ferrand, 5 rue Kessler, 63038 Clermont-Ferrand Cedex, France*
[b] *Departamento de Geología, Facultad de Ciencias Físicas y Matemáticas, Universidad de Chile- Plaza Ercilla 803, Santiago, Chile*
[c] *Institut de Recherche pour le Développement (IRD)-UR154-UMR5563 (LMTG)-UPS-CNRS-IRD, Obs. Midi-Pyrénées- 14, av. E. Belin, 31400 Toulouse, France*
[d] *Departamento de Geofísica, Facultad de Ciencias Físicas y Matemáticas, Universidad de Chile-Blanco Encalada 2002, Santiago, Chile*

Received 29 March 2006; received in revised form 4 December 2006; accepted 7 December 2006
Available online 2 February 2007
Editor: C.P. Jaupart

Abstract

ASAR-ENVISAT Interferometric Synthetic Aperture Radar (InSAR) data collected over the Lastarria-Cordon del Azufre complex (Chile–Argentina) between March 2003 and May 2005 show the persistence of the large wavelength ground inflation revealed by Pritchard and Simons in 2002 from the analysis of ERS InSAR data [Nature 418 (2002) 167–170]. After reducing the tropospheric contribution in the interferograms using a combination of data network adjustment and analysis of MODIS images, we produced an accurate interferometric time series showing a 2 yr long temporal evolution of the ground displacements patterns. Two distinct inflating signals are detected. The main signal covers an elliptical area with a 45 km NNE–SSW major axis and a 37 km minor axis. It is correlated with a regional topographic dome. We estimated its maximum inflation rate to ~2.5 cm yr^{-1}. We inverted the InSAR data for a range of source geometries (spherical, prolate ellipsoids, penny-shaped cracks). The inferred source parameters for 2003–2005 period are consistent with an over-pressured reservoir at shallow to intermediate crustal depths (7–15 km), with an average volumetric rate of inflation of about 14×10^6 m^3 yr^{-1}. In addition to this main signal a new feature highlighted by the ASAR data is short wavelength inflation (6 km wide) at the location of Lastarria volcano on the northern margin of the large wavelength signal. We explain this short wavelength signal by a spherical over-pressured source lying 1000 m below the summit of Lastarria volcano. We estimate the average volumetric rate of inflation during the observation period to be $\sim 35 \times 10^3$ m^3 yr^{-1}. It is remarkable that both volumetric variations for the large and small inflations exhibit the same evolution during the 2003–2005 period, suggesting that both processes could be related. On the basis of the inversion results and of arguments provided by field evidences and a morpho-structural analysis of the Digital Elevation Model of the area, we propose that the deep source have a magmatic origin while the shallow source is most likely related to hydrothermal fluids. In our interpretation, the on-going deformation processes observed at Lastarria-Cordon del Azufre volcanic complex could represent an evolving pre-

---

* Corresponding author. Present address: Institut de Recherche pour le Développement (IRD)-UR163-UMR6524 (LMV)-UBP-CNRS-IRD, Obs. de Physique du Globe de Clermont-Ferrand, 5 rue Kessler, 63038 Clermont-Ferrand Cedex, France. Tel.: +33 473 346 700; fax: +33 473 346 744.

E-mail addresses: froger@opgc.univ-bpclermont.fr (J.-L. Froger), remy@ird.fr (D. Remy), bonvalot@ird.fr (S. Bonvalot), denis@dgf.uchile.cl (D. Legrand).

doi:10.1016/j.epsl.2006.12.012

caldera silicic system. Further field geological and geophysical investigations will be required to confirm these hypotheses and refine the proposed model, mostly based on satellite observations.

Keywords: Interferometry; volcanoes; displacements; Lastarria; Lazufre; Andes

1. Introduction

The Central Volcanic Zone of the Andes (CVZ) includes 50 active or potentially active volcanoes distributed along a 1500 km arc between South Peru and Chile (from 15°20′S, 72°30′W to 27°20′S, 69°W, Fig. 1a) [1–4]. Most of these volcanoes are located in remote areas difficult to access and, as a consequence, are poorly known and generally not monitored using ground geophysical networks. Synthetic Aperture Radar Interferometry (InSAR) is, therefore, an appealing and appropriate alternative to volcano monitoring in the CVZ. Moreover, due to its extreme aridity, the central part of the CVZ is an exceptionally favourable natural laboratory for InSAR studies of volcanic deformation.

Using ERS data acquired between 1992 and 2000, Pritchard and Simons [5,6] achieved a large scale InSAR survey of the CVZ. They gave the first evidence of broad scale inflation and subsidence during unrest periods over few volcanic centres which where not

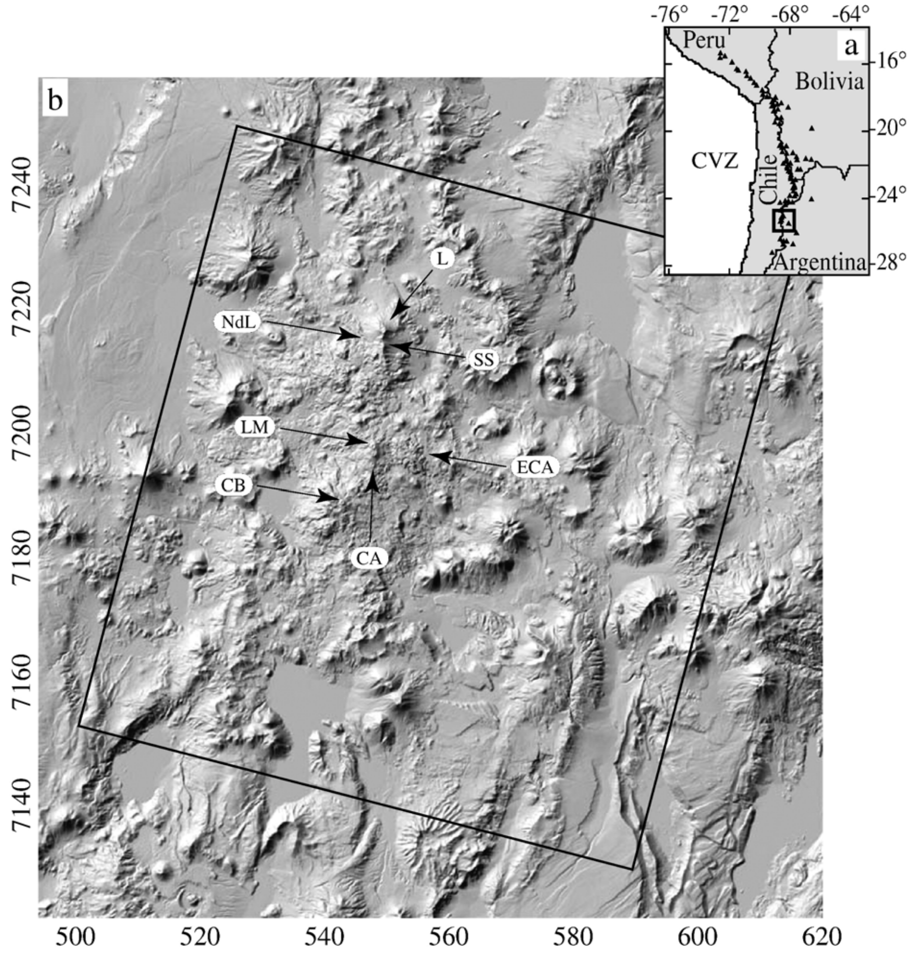

Fig. 1. (a). Location of the Lastarria-Cordon del Azufre area (black box) in the Central Volcanic Zone of the Andes. (b). Shaded DEM (SRTM) of the Lastarria-Cordon del Azufre area (CA Cordon del Azufre, CB Cerro Bayo, ECA East Cordon del Azufre, L Lastarria cone, LM La Moyra, NdL Negriales de Lastarria, SS South Spur). The black box outlines the area covered by the interferograms. Coordinates in km UTM-WGS84 (19 zone South).

previously recognized as active volcanoes. The Lastarria-Cordon del Azufre volcanic complex (Chile-Argentina) belongs to these present-day deforming volcanoes evidenced from ERS radar data [5,6]. The ground displacement signal detected there for the period 1996–2000 consists in a large elliptical (45 km in a NNE direction) inflation with a mean displacement rate of 1 cm/yr in the line of sight of the satellite [5,6]. It was interpreted in terms of over–pressured sources lying at superficial or intermediate crustal depths [5,6].

With the aim to investigate the temporal evolution of this signal (continuous or transient) we carried out a new InSAR survey with eight ASAR-ENVISAT images acquired over the Lastarria-Cordon del Azufre volcanic complex between March 2003 and June 2005. After removing external contributions (orbital, topographic and tropospheric) from the interferograms, we constructed an accurate interferometric time series which provides a refined perception of the temporal dynamics of the displacements. We present here the results of the analysis and inversion of this new interferometric dataset and discuss their implications in light of the previous results and in terms of the internal dynamics of the Lastarria-Cordon del Azufre volcanic complex.

2. Geologic setting

Lastarria (25°10′S, 68°31′W, 5706 m) and Cordon del Azufre (25°18′S, 68°33′W, 5480 m) are part of a broad polygenic quaternary volcanic complex lying on the Altiplano, on the border of Chile and Argentina (Fig. 1b). These two volcanoes are not considered as being currently active although the first is characterized by an intense fumarolic activity at its summit [7,8], and the second by two lava flows whose pristine morphologies and extremely low albedo suggest that they are young [3]. K–Ar dating gives ages of between 0.6± 0.3 Ma [9] and <0.3 Ma [10] for Lastarria and 0.3± 0.3 Ma for Cordon del Azufre [10].

Three distinct morpho-structural units form the Lastarria complex (Fig. 1b) [8,11]. The South Spur is the oldest one. It joins the Lastarria cone at the summit of the complex. The modern composite cone consists of lava flows, scoria and pyroclastic flow deposits [3]. The Negriales del Lastarria is an extended lava field located on the southwest flank of the South Spur-Lastarria cone. The eastern flank of the South Spur-Lastarria cone is cut by a prominent N–S scarp which ends to the north at the scar left by a major slope failure of the southeast flank of Lastarria cone [12]. The petrography of the Lastarria complex ranges from pyroxene andesites to pyroxene-amphibole dacites [8].

The Cordon del Azufre complex includes three morpho-structural components (Fig. 1b) [3]. To the west, the oldest part of Cordon del Azufre is made up of a chain of four craters oriented N–S. The volcano la Moyra is the most recently active centre which gave rise to a 6 km blocky lava flow to the west [3]. The third component (labelled ECA for East Cordon del Azufre in Fig. 1b) consists of a cluster of lava flows and vents lying to the east. The petrography of the Cordon del Azufre lavas ranges from hornblende-plagioclase andesites to dacites [9].

3. Data processing

3.1. Interferometric data

The eight ASAR-ENVISAT images (ASA_IMS_1P) used in this study were acquired in swath 2, V/V polarization (ERS-like mode, mean incidence angle ~23.6°), during descending passes at 14:05 local time (Table 1). We produced 28 interferograms with DIAPASON software [13] using the two-pass method described by Massonnet and Feigl [14]. Fig. 2 shows the eight ASAR images as a function of relative perpendicular baseline versus acquisition date. Each computed interferogram is represented by a line joining two images. This mode of representation mimics a geodetic network and illustrates how a global data adjustment can be performed to retrieve various parameters relative to single images from data relative to the interferograms. The contribution of the orbital trajectories in the interferograms was modelled and removed using the ESA DORIS orbit state vectors. We used the SRTM Digital Elevation Model (DEM), sampled into a 45 m pixel spacing grid, to model and remove the topographic contribution. The SRTM DEM was also used to provide a geographic frame (UTM-WGS84) for the interferometric products. The resulting interferograms span between 35 and 840 days, with altitudes of ambiguity ranging from 123 m to 12 m (Table 2).

Table 1
List of ASAR data from the ENVISAT satellite for the track/frame 2282/4119

Orbit	Date
5346	March 9, 2003
7851	Aug. 31, 2003
10857	March 28, 2004
14364	Nov. 28, 2004
15366	Feb. 06, 2005
16368	Apr. 17, 2005
16869	May 22, 2005
17370	June 26, 2005

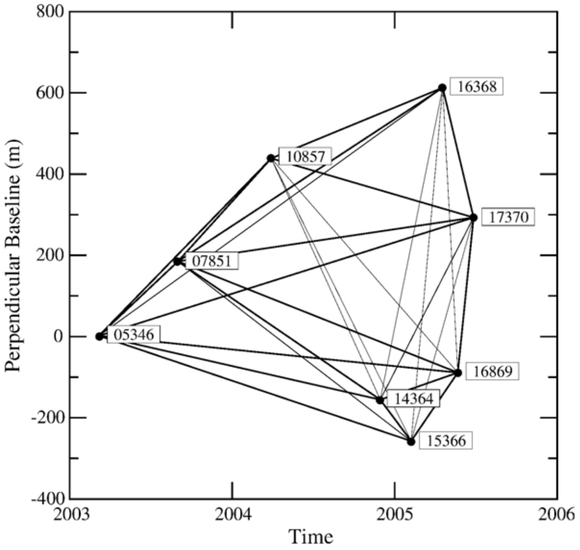

Fig. 2. ASAR image set and calculated interferograms, represented as perpendicular baseline values versus date of acquisition. Black dots and numbers are the 8 images with their associated orbit numbers. Solid lines are the 28 calculated interferograms (thick lines indicate the interferograms used for the time series generation).

3.2. Removal of orbital contribution

Most of the interferograms exhibit a regional ramp of fringes, roughly parallel to the satellite track, typical of a residual orbital contribution. We eliminated this residual contribution using a three pass approach as described here. First, we estimated the best-fitting linear ramp in space for each single interferogram. Thus we obtained two gradient values for each interferogram describing the phase variation in the range and azimuth directions (gradient values reported in Table 2). In the least good case we counted ~6 fringes/100 km in the range direction and ~2 fringes/100 km in the azimuth direction, giving a maximum error in the DORIS state vectors of 50 cm for the tangential component and 1 m for the radial component. Then, using these values relative to each interferogram, we performed a global data L2 adjustment to retrieve the optimal values, and their uncertainties, relative to each single ASAR image. Finally, we used the adjusted gradient values to calculate and remove the optimal linear ramp in each interferogram (Table 2).

3.3. Removal of tropospheric contribution

Some of our interferograms also show a clear large to medium wavelength correlation between phases and topography (Fig. 3a). Examples of such signals have been recognised previously in volcanic areas and interpreted as being mainly due to a variation in the water vapour content of the atmosphere between the different dates of acquisition [15–17]. It has been proposed that such a variation can produce phase delays strongly correlated with the elevation, provided that the atmosphere is vertically layered and horizontally homogeneous [16,18]. In this case, the atmospheric phase delays can be adequately modelled, directly from the interferograms, by adjusting the phase-elevation relation with a linear, polynomial or exponential function [16]. On the contrary, turbulent atmosphere produces uncorrelated short to medium wavelength phase delays that are generally much more difficult to model [19,20].

We were able to investigate the structure of the atmospheric signal by analyzing the independent information provided by a set of 8 MODIS images (Moderate Resolution Imaging Spectroradiometer) acquired over the Lastarria-Cordon del Azufre area between 5 and 70 min after the ASAR acquisitions.

From each MODIS image we extracted a map of the Precipitable Water Vapour (PWV). The PWV maps could theoretically be used to correct the atmospheric phase delay in the interferograms, on a pixel-by-pixel basis, following the approximations proposed by [15,17,21]. We did not retain this approach for three main reasons: (a) the MODIS data do not provide an image of the atmosphere PWV at the exact time of the ASAR acquisition; (b) the horizontal resolution of the MODIS data is low (~1 km) with respect to the one of the ASAR images (typically some tens of metres); and (c) some of our MODIS images have a high percentage of missing data (between 27% and 86% depending on the image).

However, we believe that the MODIS data can provide a reliable estimation of the general atmospheric structure (i.e. mostly layered, or turbulent) which, in the context of the Altiplano, is unlikely to change critically between the ASAR and the MODIS acquisition.

In most of the cases, the MODIS inferred atmospheric phase delays exhibit a clear correlation with elevation. Theoretical models of water vapour content in layered atmosphere generally assume a non linear decrease with altitude [15]. But here, because of the high base altitude (3.5 km) of the relief, the effects of the exponential decay are barely noticeable and the phase delay-elevation correlations appear linear at the first order and roughly constant over the whole area. The typical phase-elevation gradient ranges between 0.01 and 0.5 fringe per 2000 m with rms between 0.10 and 0.17 fringes per 2000 m (2000 m is the elevation range

Table 2
Parameters associated with the 28 interferograms

Master image	Slave image	ΔT[a]	AA[b]	$\delta\Phi/\delta x_{est}$[c]	$\delta\Phi/\delta x_{calc}$[d]	$\delta\Phi/\delta y_{est}$[e]	$\delta\Phi/\delta y_{calc}$[f]	$\delta\Phi/\delta z_{MODIS} \pm 1\ \sigma$[g]	$\delta\Phi/\delta z_{est}$[h]	$\delta\Phi/\delta z_{calc}$[i]
05346	07851	175	−74	−3.29	−3.28	0.13	0.15	−0.34±0.14	−0.22	−0.17
05346	10857	385	−29	−5.45	−5.45	0.78	0.77	−0.26±0.13	−0.29	−0.29
05346	14364	630	52	−1.40	−1.41	0.21	0.24	0.16±0.14	0.13	0.12
05346	15366	700	36	0.75	0.83	0.50	0.55	−1.79±0.65	−1.59	−1.66
05346	16368	770	−19	−0.82	−0.88	−1.36	−1.37	0.15±0.10	0.16	0.23
05346	**16869**	805	91	−0.72	−0.74	−0.23	−0.28	−0.23±0.12	−0.29	−0.29
05346	**17370**	840	−36	−2.08	−2.11	1.02	1.04	−0.12±0.11	−0.31	−0.27
07851	10857	210	−46	−2.18	−2.18	0.62	0.62	0.08±0.16	−0.15	−0.12
07851	14364	455	30	1.93	1.87	0.07	0.08	0.50±0.17	0.31	0.29
07851	15366	525	24	4.07	4.10	0.36	0.40	−1.45±0.65	−1.49	−1.49
07851	16368	595	−25	2.40	2.40	−1.52	−1.52	0.49±0.13	0.36	0.40
07851	**16869**	630	40	2.54	2.54	−0.40	−0.43	0.11±0.15	−0.08	−0.11
07851	**17370**	665	−71	1.17	1.16	0.89	0.88	0.22±0.15	−0.17	−0.10
10857	14364	245	18	4.05	4.05	−0.52	−0.53	0.42±0.16	0.40	0.41
10857	15366	315	16	6.26	6.28	−0.24	−0.22	−1.53±0.65	−1.42	−1.38
10857	16368	385	−56	4.62	4.57	−2.14	−2.14	0.41±0.12	0.40	0.51
10857	16869	420	21	4.69	4.71	−1.01	−1.05	0.03±0.14	0.10	0.00
10857	17370	455	125	3.40	3.34	0.24	0.27	0.14±0.13	−0.01	0.02
14364	15366	70	117	2.24	2.23	0.25	0.31	−1.95±0.65	−1.76	−1.78
14364	16368	140	−14	0.62	0.53	−1.59	−1.61	−0.01±0.13	0.09	0.10
14364	16869	175	−123	0.67	0.67	−0.51	−0.52	−0.39±0.15	−0.42	−0.41
14364	17370	210	−21	−0.74	−0.71	0.82	0.80	−0.28±0.15	−0.37	−0.39
15366	16368	70	−12	−1.79	−1.70	−1.94	−1.92	1.94±0.65	2.03	1.89
15366	16869	105	−60	−1.55	−1.57	−0.89	−0.83	1.56±0.65	1.31	1.38
15366	17370	140	−18	−2.98	−2.94	0.50	0.49	1.67±0.65	1.40	1.40
16368	16869	35	15	0.13	0.14	1.09	1.09	−0.38±0.11	−0.42	−0.51
16368	17370	70	38	−1.24	−1.23	2.38	2.41	−0.27±0.10	−0.43	−0.49
16869	17370	35	−26	−1.34	−1.37	1.31	1.32	0.11±0.13	0.05	0.02

Interferograms used for best fitting source location are indicated in bold (see section 4.2.2).

[a] Time spanned by the interferogram in days.

[b] Altitude of ambiguity in m.

[c] Estimated residual orbital phase gradient in the range direction in fringes per 100 km.

[d] Calculated residual orbital phase gradient in the range direction in fringes per 100 km (global data L2 adjustment).

[e] Estimated residual orbital phase gradient in the azimuth direction in fringes per 100 km.

[f] Calculated residual orbital phase gradient in the azimuth direction in fringes per 100 km (global data L2 adjustment).

[g] Phase/elevation gradient in fringe per 2000 m and its standard deviation deduced from MODIS PWV estimations.

[h] Phase/elevation gradient in fringe per 2000 m estimated from InSAR data.

[i] Phase/elevation gradient in fringe per 2000 m calculated by global L2 adjustment of the estimated values.

in the studied area) (Table 2, Fig. 3b and c). This general behaviour validates the hypothesis of a mostly vertically layered and horizontally homogeneous atmosphere with low PWV variations between the different acquisitions. However, the phase delays calculated for the combinations including the February 2005 MODIS image differ slightly from this simple behaviour. The phase-elevation gradients are significantly higher (between 1.45 and 1.95 fringes per 2000 m) indicating a higher PWV content in the atmosphere, while the higher rms values (0.65 fringes per 2000 m) reflect the horizontal variability of the PWV indicating a turbulent component in the atmospheric signal. February corresponds to the end of the austral summer wet period, during which the Altiplano is affected by easterly wind anomalies in the middle and upper troposphere, resulting in increased moisture influx from the interior of the continent [22].

Nevertheless, the analysis of the MODIS data demonstrates that a simple linear fit of the phase-elevation relation can generally be used to correct, at least to the first order, most of our interferograms. Therefore, we estimated the phase-elevation gradient directly from each interferogram (Fig. 3d). We then performed a global data L2 adjustment, using a similar approach to that used for the correction of orbital residuals, in order to retrieve the gradient for each ASAR image. Finally, we used these retrieved gradients to calculate and remove an optimal atmospheric phase screen from each interferogram (Table 2).

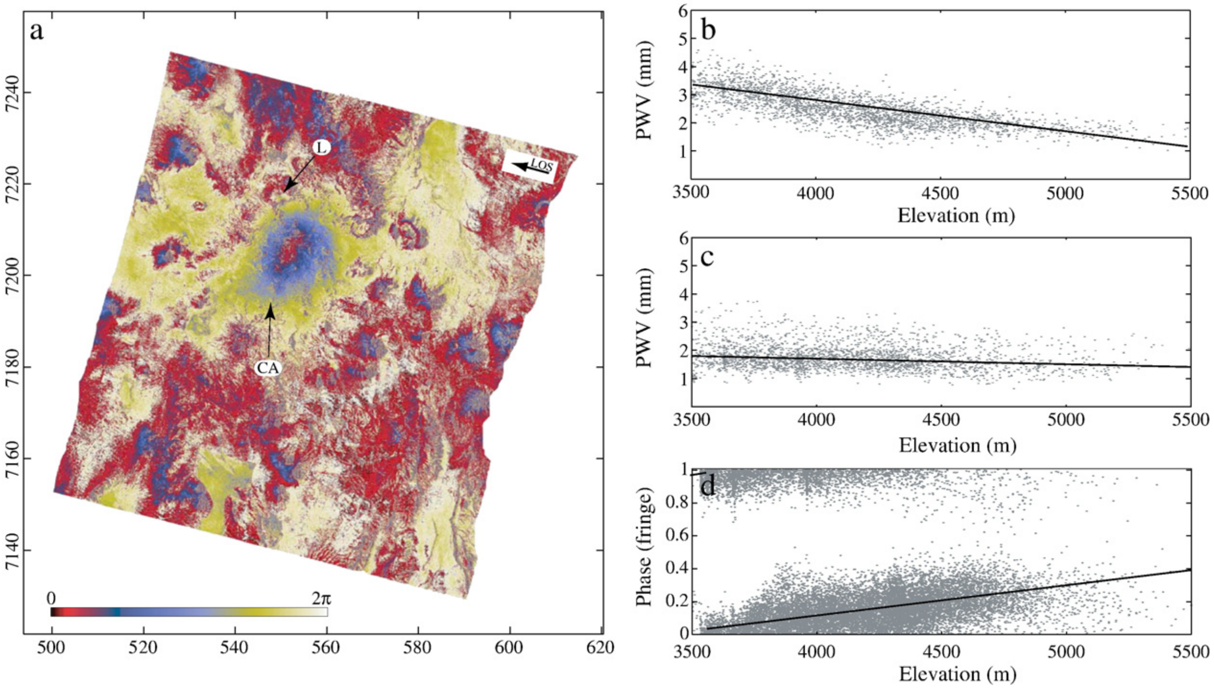

Fig. 3. (a). Interferogram spanning 385 days from 28 March 2004 to 17 April 2005. A complete cycle of phase (blue-red-yellow) represents a decrease in range of 2.8 cm between the ground surface and the satellite. The phase-elevation correlation is evident when the interferogram is compared with topography of Fig. 1b. The yellow to red elliptic fringe pattern between Lastarria (L) and Cordon del Azufre (CA) is the Lazufre signal. Coordinates are in km UTM (19 zone South). (b). MODIS inferred PWV values as a function of elevation for 28 March 2004 (thick line corresponds to the best linear fit). (c). MODIS inferred PWV values as a function of elevation for 17 April 2005. (d) Phase-elevation data extracted for the most coherent pixels of the ASAR interferogram displayed in (a). The solid line is the modelled wrapped phase delay. In this example, both MODIS inferred phase elevation gradient (0.41 fringe per 2000 m) and the one estimated directly from the interferogram (0.40 fringe per 2000 m) are very close thus demonstrating the good agreement between the two independent dataset.

3.4. Corrected interferograms

After correction, all the interferograms spanning more than a 35 days period exhibited a prominent large wavelength phase signal with variable amplitude, elongated in the NNE–SSW direction. A pairwise logic analysis shows that this signal can be interpreted only as a broad displacement of the ground in the satellite direction. Its amplitude is maximum on the interferogram displayed in Fig. 4a that spans a 840 days time between March 2003 and June 2005 (the longest time spanned with our InSAR dataset). As expected, this interferogram is extremely coherent without any noticeable orbital, topographic or tropospheric residual. The observed phase signal reaches up to 2 fringes and covers an elliptical area with a 45 km NNE–SSW major axis and a 37 km minor axis. It corresponds remarkably in location and shape with the displacement pattern previously detected over the Lastarria-Cordon del Azufre area for the 1998–2000 period by Pritchard and Simons [6]. Its actual extension, however, appears to be slightly increased to the south west, including, in particular, the Cerro Bayo volcano (K–Ar age: 0.8 ± 0.1 Ma [10]). Hereafter, following the Pritchard and Simons [6] terminology, we refer to this large wavelength signal as the Lazufre signal.

A new feature, with respect to the previous observations, is the presence of a smaller fringe pattern, 6 km wide, at the location of Lastarria cone, on the northwestern margin of the Lazufre signal (Fig. 4b). This fringe pattern is compatible with an upward displacement of the ground in the satellite direction. Hereafter, we refer to this short-wavelength signal as the Lastarria signal.

4. Deformation modelling

4.1. Time series analysis of displacements at Lazufre

In order to understand and quantify the time dependency of displacements better, we generated a time series relative to the earliest SAR image of our data set (March 2003) using the technique proposed by

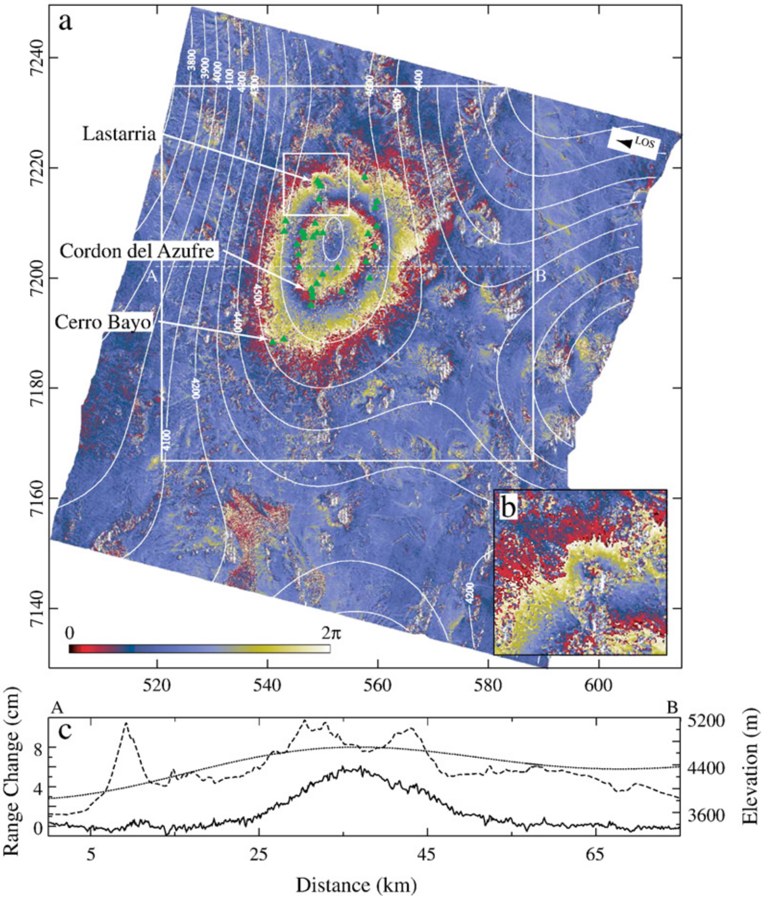

Fig. 4. (a). Interferogram spanning 840 days from 9 March 2003 to 26 June 2005. The white boxes outline the areas where time series analysis and modelling were performed. White contours show the large wavelength topography obtained by filtering a 365×365 km extraction of the SRTM-90 DEM, centered over the Lastarria-Cordon del Azufre area. We used a low-pass filter that damps topographic variation over spatial scales below 75 km. Note the coincidence of the Lazufre signal with a regional topographic dome. Green triangles mark the location of quaternary volcanoes deduced from morpho-structural analysis of SRTM and Landsat imagery. Coordinates are in km UTM (19 zone South). (b). Enlargement of the Lastarria cone area. (c). Unwrapped LOS displacements (thick line) along the profile A–B shown in (a). Dashed line indicates the elevation along the profile and dot line corresponds to the filtered large wavelength topography along the profile.

Lundgren et al. [23]. First we unwrapped the interferograms using the Snaphu algorithm [24]. Due to the exceptional aridity of the area, all the interferograms exhibit an excellent coherence and the unwrapping step is easily achieved without any noticeable errors. Then, in order to make the phase values comparable in both space and time, we selected a reference point outside of the area affected by displacements. Each interferogram is then corrected for a constant shift calculated as the mean phase in a 64×64 pixel window centred on the reference point.

Next we inverted an InSAR data network, formed by a subset of 18 interferograms selected as the more coherent (altitude of ambiguity greater than 25 m, see Fig. 2 and Table 2). In this way, for a given pixel, the observed displacement is adjusted to minimize the closure discrepancies within the network. The temporal evolution of the displacement field is shown in Fig. 5 where each image corresponds to the adjusted displacement field relative to the earliest one.

Fig. 6 shows the time series of the maximum uplift calculated as the mean of displacements in a 20×20 pixel window centred on the area of maximum displacement. The maximum uplift reaches up to 57 mm±3 mm between March 2003 and June 2005. The trend is remarkably linear with a mean displacement rate of 2.5 cm yr^{-1}. This value is significantly higher than the 1 cm yr^{-1} estimated by Pritchard and Simons [6] for the 1996–2000 period. However, as suggested by these authors, their rate is probably underestimated as no

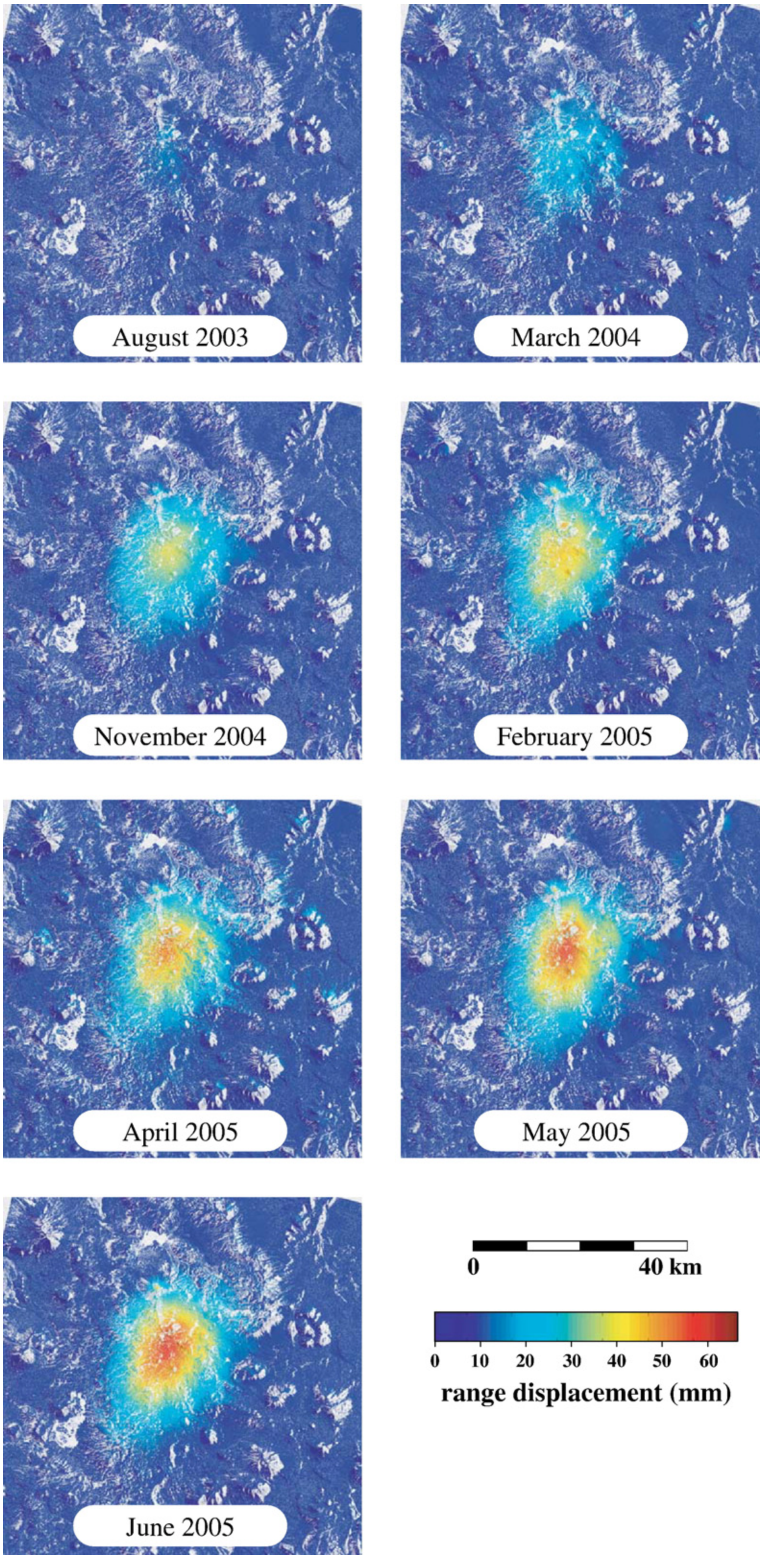

Fig. 5. Inverted displacement field at Lazufre for each of the 7 ASAR images relative to the earliest one (March 2003) (displacement toward the satellite are positive). Areas where the interferometric coherence is lost are shown in grey.

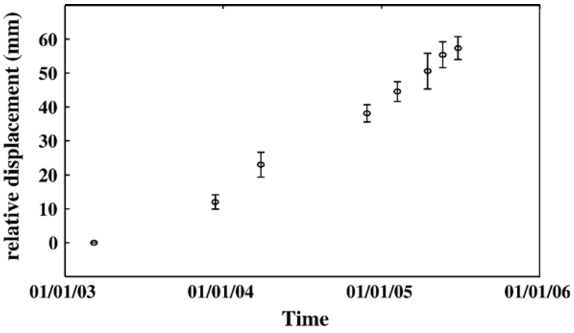

Fig. 6. Time series of maximum displacements for Lazufre signal relative to the earliest image (displacement toward the satellite are positive). Vertical bar is the mean standard deviation in a 20 × 20 pixel window centred on the area of maximum displacement.

displacement was observed before 1998. This suggests that the geophysical process responsible for the 1998–2000 displacement has continued up to the present day, possibly with acceleration in the uplift.

4.2. Modeling displacements at Lazufre

4.2.1. Hypothesis and a priori constrains

Our InSAR data set provides a measure of the surface displacements in the line of sight of the satellite. Without any complementary constraint, the inversion of a single component of the displacement vector does not allow a unique determination of the source characteristics. Therefore, in order to find acceptable models, we decided to explore a range of possible source geometries (e.g. spherical, prolate ellipsoids, and penny-shaped cracks) similar to those investigated in the previous studies of Pritchard and Simons [6]. In this way, our results can be directly compared with those obtained by these authors for the 1998–2000 period. Each of the investigated source models has a simple analytical solution for surface displacements [25–27] expressed as a function of the source location (*X*, *Y*, *Z* coordinates), its dimensions (radii or lengths of semi-major and semi-minor axes), its orientation (strike, dip) and a strength (over-pressure). However, simulations with synthetic data show that an important limitation of such analytical models is the intrinsic trade-off between some model parameters. Depth and dimensions of the source both influence the wavelength of the displacements while strength and volume of the source both influence the amplitude of the displacements. This leads us to some simplifications to avoid misinterpretations and ease the comparisons with the previous modelling proposed for the Lazufre signal [6]. For the spherical source we considered a point source (radius $\ll$ depth) and inverted for the location and strength of the source. For the ellipsoids (horizontal or vertical) we fixed the length of the semi-major axis and the length ratio between semi-major axis and semi-minor axis to the value found by Pritchard and Simons [6], and we inverted for the location, orientation and strength. For the penny-shaped cracks (point cracks or finite cracks) we fixed the radius of the source to the value found by Pritchard and Simons [6], and we inverted for the location and strength.

Another drawback of analytical models is the neglect of topographic effects [28]. In our case, the large wavelength of the signal indicates that the source is probably relatively deep. Therefore, as a simplification, we assumed that the real topography can be approximated by a horizontal plane without modifying significantly the modelled displacements. Further model sophistications, such as accounting for complex rheological crustal structure, do not appear to be relevant here. Pritchard and Simons [6] stressed that the rheological structure of the crust in the central Andes is poorly constrained and showed that accounting for complex rheology does not significantly change modelling results. Therefore, we assumed that the source is in a homogeneous isotropic Poissonian elastic half-space.

4.2.2. Inversion method

For each source geometry we solved firstly for the best fitting source location from a subset of four interferograms (indicated in bold characters in Table 2) using a genetic algorithm [29]. In order to reduce the computational cost of the inversion, we first sampled the data using a quadtree partitioning approach [30]. In this approach the interferogram is recursively divided into quadrants the size of which decreases until the variance of the data within each quadrant is below a fixed threshold. For the four selected interferograms, we carried out an analysis of the covariance structure of the noise. The amplitude of the noise varies between 3 mm^2 and 5 mm^2. These low values again confirm the remarkable horizontal homogeneity of the troposphere since turbulent troposphere typically gives noise amplitude which is one to two orders of magnitude higher (see for example [30,31]). In agreement with these results we fixed the threshold value for the quadtree partitioning to four times the maximum noise variance i.e. 20 mm^2. The initial and sampled signals used for the data inversion are shown in Fig. 7.

In order to be able to compare with previous results [6] we performed two series of modelling. In the first one we fixed all the parameters, except the strength, to the values obtained by Pritchard and Simons [6] for the 1998–2000 displacements and inverted for the strength.

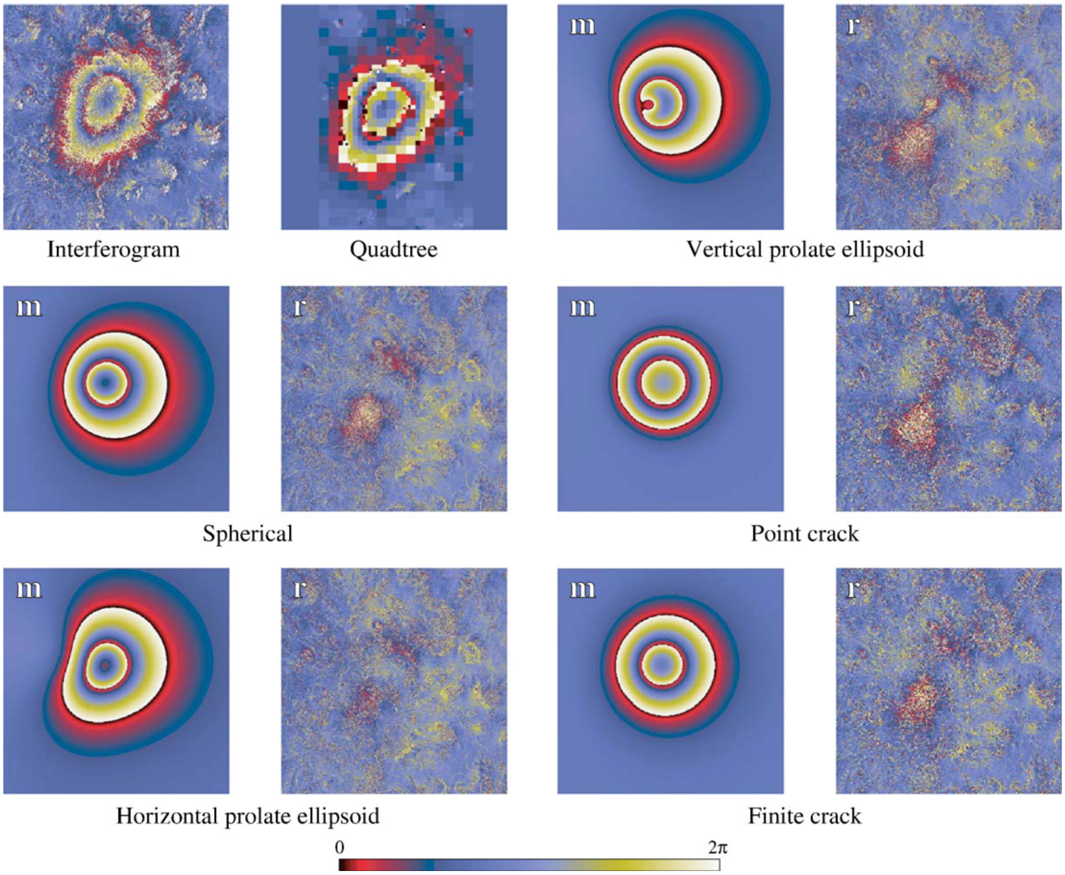

Interferogram

Quadtree

Vertical prolate ellipsoid

Spherical

Point crack

Horizontal prolate ellipsoid

Finite crack

Fig. 7. Modelling results for the 9 March 2003 to 26 June 2005 interferogram. (m) models; (r) residuals. Models and residuals are rewrapped.

In the second series, we just fixed the dimension of the sources to the values found by Pritchard and Simons [6] and inverted all the others parameters. Table 3 shows the best fitting source characteristics for the different geometries and Fig. 7 shows the models and residuals for the March 2003–June 2005 interferogram. The parameters and root mean square errors (RMSE) in Table 3 are estimated by the weighted average of the values obtained for each of the four interferograms.

4.2.3. Results

Our solutions for the spherical source, the vertical prolate ellipsoid or the penny-shaped cracks fit reasonably well the data with residual RMSE ranging between 4 mm and 5 mm (Fig. 7). However, they do not match the displacement pattern as well as the solution for a horizontal prolate ellipsoid (Fig. 7). All the models exhibit two main areas of residuals located to the NE and SW of the source centre position, indicating that the wavelength of modelled displacement is too short in the major-axis direction of the signal. A slightly higher shape ratio (a/b in Table 3), for the horizontal prolate ellipsoid, could probably allow us to adjust the data more satisfyingly. The only significant difference we found between our best models and the models for which location, dimensions and orientation are fixed to the values found by Pritchard and Simons [6] concerns the depth of the sources. Our sources are systematically shallower, with differences ranging between 1 and 5 km. As the dimensions of the sources are fixed, there is no trade-off between the depth and the other parameters. Thus the depths of our models are relatively well constrained and we can assume that the systematic difference with the previous study is significant. This difference cannot be satisfyingly explained by a rising of the source between 1998–2000 and 2003–2005, as this would require a rate of rise of between 200 m and 1000 m/yr. Such a large rate of rise seems neither to be geologically realistic nor does it appear consistent with our data. It would induce a perceptible change in the depth of the source during the time of our InSAR survey, which we do not observe when comparing the depth

Table 3
Summary of the best fitting source characteristics for different geometries in an elastic half-space[a]

	Spherical		Horizontal ellipsoid		Vertical ellipsoid		Point crack		Finite crack	
Longitude	549.5	549.9±0.3	549.9	549.2±0.3	545.4	548.2±0.3	553.9	550.5±0.2	553.7	550.8±0.2
Latitude	7204.9	7205.9±0.4	7204.5	7204.7±0.3	7206.0	7204.2±0.3	7204.1	7205.6±0.3	7203.9	7205.4±0.3
Z	12.1	10.3±0.5	14.6	9.6±0.6	11.2	7.1±0.4	17.6	15.2±0.7	10	8.8±0.6
a/*b*	–	–	9.5	9.5	4.3	4.3	–	–	–	–
ϕ	–	–	E22°N	E25°N±7	W24°N	–	–	–	–	–
θ	–	–	−1.2	9°±2	109°	90°±0.5	–	–	–	–
Radii	–	–	–	–	–	–	1.0	1.0	13.4	13.4
RMSE	5.1	4.7	6.8	4.3	6.3	5	8.4	4.4	8.2	4.5

[a] The latitude and longitude are expressed in km (UTM WGS84 zone 19 South). *Z* is the depth in km below the mean surface elevation (i.e. 4550 m a.s.l.). *a*/*b* is the length ratio between major and minor axis for ellipsoidal sources. ϕ and θ are respectively the strike and the dip of ellipsoidal source. Radii are in km. For each source geometry we indicate in the left-hand column the parameter values for the "Pritchard and Simons like" source and in the right-hand column the weighted averaged parameter values, and their associated confidence intervals (1 σ), for our best models. The weight is given by n_i/NTOT, where n_i is the number of observations for the i^{eme} interferogram (taken in the set of the four selected interferograms) and NTOT is the total number of observations. The root mean square values of the residuals (RMSE), expressed in mm, are determined using the following formula:

$$\mathrm{RMSE} = \sqrt{\frac{1}{\mathrm{NTOT}}\sum_{i=1}^{4} n_i(\mathbf{X}_\mathrm{o}-\mathbf{X}_\mathrm{c})^2}$$

where $\mathbf{X}_\mathrm{o}$ and $\mathbf{X}_\mathrm{c}$ represent observed and predicted displacements respectively.

values inferred from the inversion of our interferograms for the 2003–2004 and 2004–2005 periods, respectively.

An alternative explanation for the observed differences could be that the wavelength of the signal in the 1996–2000 interferograms used by Pritchard and Simons [6] is artificially increased by an atmospheric contribution correlated with the topography. Thus, a deeper source would be required to adjust the displacements. We checked this hypothesis with the March 2003–February 2005 interferogram where the atmosphere is responsible for about 0.5 fringe in addition to the displacement fringes in the Lazufre area. We inverted both the initial interferogram and the one corrected for the atmosphere, fixing all the parameters except the depth and the strength to the values found for the better horizontal ellipsoid model. For a similar strength, the best model found for the uncorrected interferogram has a depth approximately 4 km deeper than for the corrected interferogram (respectively 14 km and 10 km). This result emphasizes the importance of accounting for possible atmospheric contribution in the interferograms before any modelling approach.

In a next step, we estimated the volume changes that could explain the observed temporal evolution of the inflation. In the case of a spherical source, the volume change ΔV of the source can easily be obtained from the relation:

$$\Delta V = \frac{\pi r^3 \Delta P}{\mu}$$

[32] where ΔP is the change in pressure along the surface of the spherical magma chamber, r is the radius of the chamber, μ is the shear modulus and $\Delta P r^3/\mu$ is the inverted source strength. Thus, assuming a constant depth equal to the one previously determined for the best spherical model, we solve the volume change within the source for the 18 interferograms of our InSAR data network. Then we used the same approach as for the time series calculus to obtain a value of volume change for each ASAR image relative to the earliest one. Fig. 8 shows the inferred volume change as a function of time. The rate of volume change is roughly constant during the March 2003–June 2005 period, with a mean value of $13.9 \pm 0.3 \times 10^6$ m^3 yr^{-1} (i.e. approximately twice the

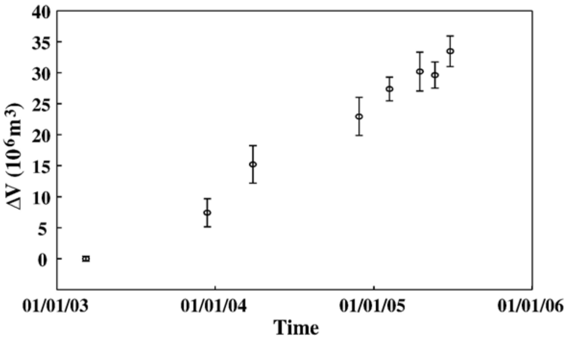

Fig. 8. Volume change inferred for the Lazufre signal assuming a spherical source at constant depth in elastic half space. Error bars indicate the standard deviation resulting from the least square adjustment.

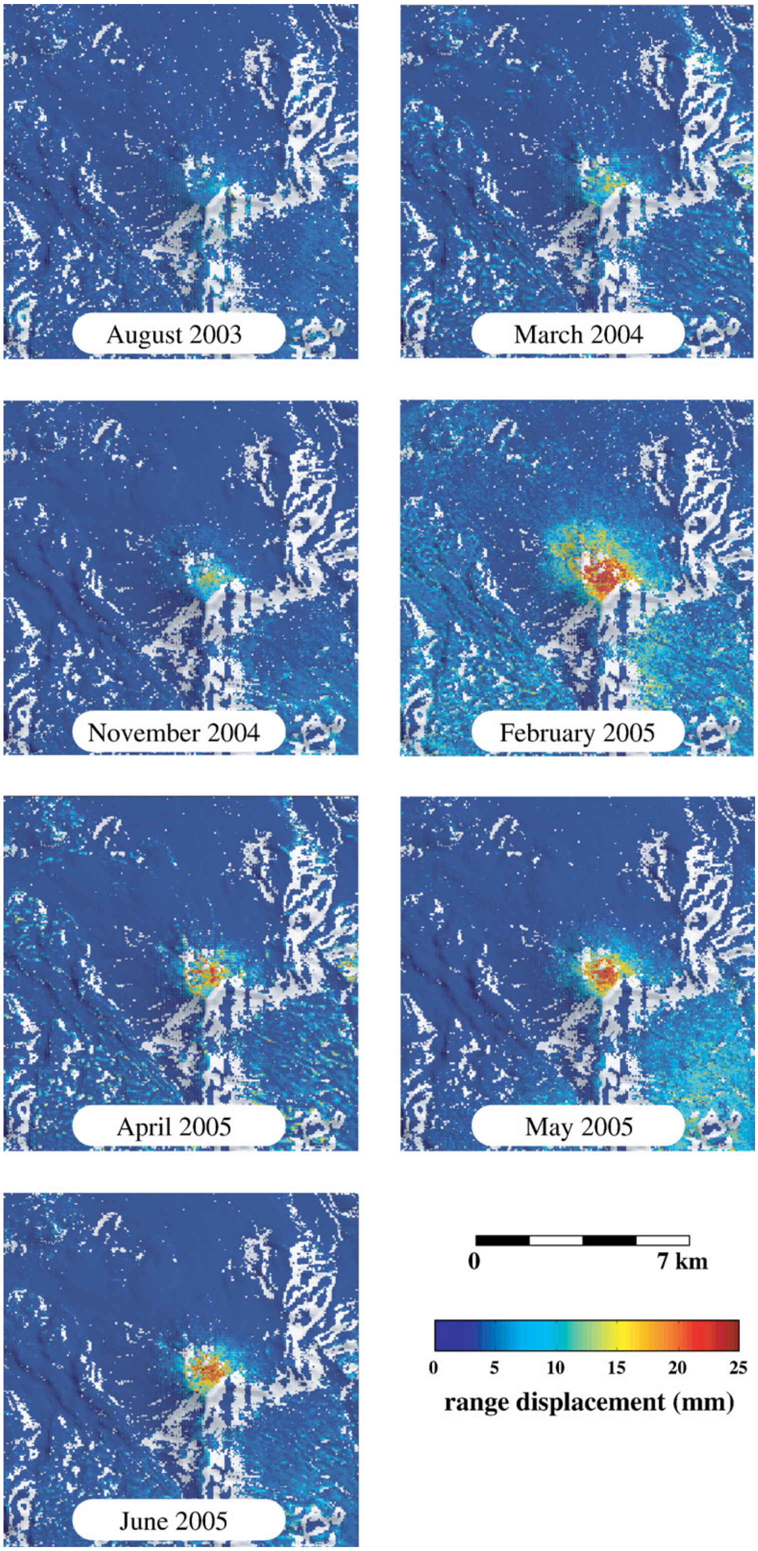

Fig. 9. Inverted displacement field at Lastarria for each of the 7 ASAR images relative to the earliest one (March 2003) (displacements toward the satellite are positive). Areas where the interferometric coherence is lost are shown in grey.

rate obtained by Pritchard and Simons for the 1996–2000 period).

4.3. Time series analysis and modelling of displacements at Lastarria

The short-wavelength displacements observed on the Lastarria cone are superimposed on a regional trend due to the influence of the large wavelength Lazufre signal. So, in order to analyse the Lastarria signal properly, we corrected the interferograms for the best-fitting model obtained for the Lazufre signal (i.e. the horizontal prolate ellipsoid). Then the residual displacements were adjusted in order to produce a time series using a similar approach to that presented in Section 4.1. The results, shown in Fig. 9, confirm the presence of a subtle, but consistent, pattern of displacement, centred over Lastarria. Fig. 10 shows the derived time series of maximum uplift. The amplitude of the uplift was calculated as the mean value of a 10 × 10 pixel window centred on the area of maximum uplift. The trend is roughly linear with a rate of 9 mm yr^{-1} and a maximum uplift of 25 mm between March 2003 and June 2005. However, the value obtained for February 2005 shows a significant deviation from the general trend. We believe that this apparent increase in the uplift is mainly due to signal contamination by local atmospheric heterogeneities, which are not corrected for in our approach (see previous discussion about the atmospheric signal in the February 2005 image).

The similarity in temporal evolution of the maximum uplifts at Lastarria and Lazufre suggests that the two responsible processes, although occurring at different spatial scales, are related. Pritchard and Simons [6] did not notice displacements at Lastarria during the 1996–2000 period. One reason could be that the beginning of the displacements at Lastarria was delayed with respect to those observed at Lazufre.

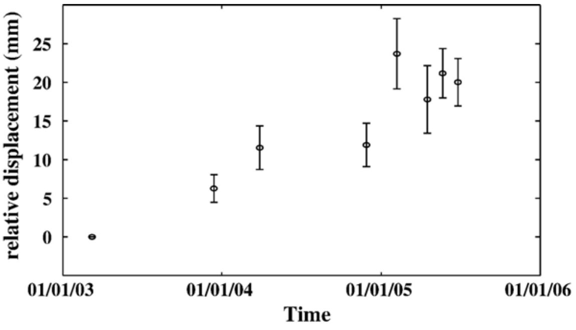

Fig. 10. Time series of maximum displacements for Lastarria signal relative to the earliest image (displacements toward the satellite are positive). Vertical bar is the standard deviation in a 10 × 10 pixel window centred on the area of maximum displacement.

We inverted the Lastarria signal in order to find the best spherical source. As the wavelength of the displacements is short with respect to the Lastarria cone dimensions, we expected a source located at a shallow depth inside the cone. In this case, the topography would have a significant influence on the shape of the displacement field. Taking this constraint into account, we modelled the displacement using a 3-D Mixed Boundary Element Method [28] which incorporates realistic topography. We reproduced more than 65% of the observed displacements with a source located ~1000 m below the Lastarria summit and a volume change rate of 35×10^3 m^3 yr^{-1}.

5. Discussion and conclusions

We explain the displacements at Lazufre as being due to an over-pressured source lying between 7 and 15 km below the surface. The InSAR data alone do not allow the exact nature of this source to be determined. A variety of mechanisms have been invoked in previous studies to explain uplift of the ground surface in volcanic areas. They include volume increase of a magmatic reservoir by influx of new magma [33], pressure increase of volatiles within a magmatic reservoir as a consequence of fractional crystallization [34], or thermal expansion due to partial melting of crustal rocks surrounding a magmatic reservoir [35]. Another mechanism invoked, in particular to explain uplift (or subsidence) in large caldera settings such as Yellowstone, Long Valley or Campi Flegrei, is an increase (or decrease) of pressure in a sealed geothermal reservoir [36–38]. At Lazufre, there is no clear evidence of a large caldera depression that can serve as a structural trap for a geothermal field. The scarp at the eastern flank of the South Spur-Lastarria cone could perhaps represent the remnant of a caldera wall, but there is no obvious spatial relation between this structure and the Lazufre displacements pattern. Surface manifestations classically associated with a geothermal field, such as hot springs or thermal pools, have not been reported for the Lazufre area, except at the very localised place of the Lastarria summit where fumarolic activity has been observed [3,6]. However, due to the low visit frequency of this remote and uninhabited area, discrete geothermal manifestations could have escaped detection. Thus, although a purely geothermal origin appears unlikely, additional field investigations such as seismic monitoring, or PS monitoring are needed in order to rule out definitively (or not) a hydrothermal origin.

Pritchard and Simons [6] did not observe any displacement at Lazufre before the beginning of 1998. Then the uplift rate increased rapidly. Between March

2003 and June 2005, the almost constant uplift rate of 2.5 cm yr^{-1} deduced from our data suggests a smooth steady-state continuation of this process. Unfortunately we are unable to assess its dynamic between 2000 and 2003 due to the lack of InSAR data during this period. The partial melting of country rocks by diffusion of heat from a cooling magma body is expected to have a strong temporal inertia. As a consequence, the rapid initial increase of the uplift rate hardly appears compatible with such a process. On the contrary, a new input of magma within a reservoir can induce, firstly, a sudden geometric expansion of the reservoir, and then a continuous increase in pressure, at a constant rate, due to the progressive over-saturation of volatile species released by fractional crystallization. An alternative is one in which the pressure increase in the magmatic reservoir could be directly induced by an external event, like the distant M_w 7.1 subduction zone earthquake mentioned by Pritchard and Simons for example, without any need of a new input of magma.

A careful morpho-structural analysis of the SRTM DEM and Landsat imagery of the Lazufre area provides also some indications about the possible nature of the source of the displacements. The Lazufre signal appears to be superimposed on a large regional topographic dome ~500 m high, crowned by a ring of quaternary cones, domes and lava flows (including Lastarria and Cordon del Azufre, Fig. 4a and c). The volcanic ring surrounds a central depression previously noted by Pritchard and Simons [5]. Such an association of a regional dome with a concentric pattern of volcanoes evokes some of the structural features identified by Lipman [39] as typical of a pre-collapse stage in a general caldera cycle. In the Lipman model, the regional doming is explained by upward movement and accumulation of a large body of silicic magma in the crust. The concentric pattern of volcanoes could reflect a concentration of tensile stress at a certain radial distance from the top of the magma body, where injections could preferentially initiate [40].

As a consequence, we propose that the Lazufre signal could be the evidence of the growth of a large silicic magma chamber beneath this part of the central Andes Altiplano. New input of basaltic magma, from the upper mantle and/or lower crust, into the base of the magma chamber could induce both an expansion of the chamber and a fractional crystallisation episode that would release volatiles and thus contribute to an increase in the pressure. The expansion of the chamber and the pressure increase are accommodated elastically by the crust and result in uplift of the ground surface. Episodically, when the pressure rises sufficiently to fracture the surrounding rocks, magma injection could propagate to a shallower reservoir or directly to the ground surface where it would produce an eruption.

In this interpretation, all the edifices forming the volcanic ring around the centre of the Lazufre signal would have been built by eruptions fed by the deep Lazufre reservoir either directly or indirectly via an intermediate shallow reservoir. This implies on one hand that a common geochemical heritage (which remains to be investigated) should exist between all these volcanoes, and on the other hand that the deep Lazufre reservoir has been active at least since the first eruptions of the oldest volcano in the ring. Although only few datations are available for the area, the age's range and their uncertainties (between 0.8 and <0.3 Ma) are compatible with the typical life time of a large silicic magma chamber.

A migration and accumulation of magma from the deep reservoir of Lazufre to a shallower reservoir beneath the Lastarria cone is a seducing scenario to explain the short wavelength inflation detected there. However, considering the shallow depth of the source as inferred from our best model (~1000 m), hydrothermal fluids are more likely to play a predominant role in the ongoing inflation than magma. Thus the process responsible for the Lastarria signal could be the pressurization of a partially sealed hydrothermal system similar to, but smaller than, the ones observed at Yellowstone, Long Valley or Campi Flegrei [36–38]. The intense fumarolic activity observed at the Lastarria summit is consistent with this interpretation. A geochemical survey of the fumarolic gazes emitted by the Lastarria would help to discriminate between a meteoric or a magmatic origin of the fluids. In the first case, the high geothermal flux required to pressurize the hydrothermal system could comes from the heat produced by the Lazufre magma chamber. In the second case, the fluids of the hydrothermal system could have been directly released from the Lazufre magma chamber and the Lastarria would behave as a sort of “valve” for the entire system.

Whether the displacements detected at Lazufre and Lastarria are premonitory signals of a future eruption is not known. Thus, although the area is unpopulated in a 150 km radius, it is important to maintain a minimum monitoring. As illustrated by our study, this could be achieved using InSAR which is an ideal method in this terrain for the monitoring of dynamic processes. Complementary monitoring techniques, such as GPS, microgravity and broadband seismometers, will also be useful in order to obtain tighter constraints on the nature the geometry and the dynamics of the displacement sources. New ASAR data acquired in June 2006 showed that surface displacements continued both at Lazufre and Lastarria at essentially the same rate as in previous years.

Acknowledgements

The authors would like to especially thank Fran Van Wyk de Vries for early reviews of this manuscript. We are grateful to Claude Jaupart and an anonymous reviewer for thoughtful comments. Fruitful conversations with J.-F. Lénat, P. Labazuy and V. Cayol help us to improve the manuscript. We also thank P. Lundgren and Y. Fialko for providing us with their Matlab programs for Yang and penny-shaped cracks models. ASAR-ENVISAT images were provided by the European Space Agency through the projects ENVISAT-AO #857 and Category 1 #2899. This work was supported by IRD (Dept. DME) and the FONDECYT/CONICYT n°1061253 (Chile).

References

[1] S.L. De Silva, Altiplano-Puna volcanic complex of the central Andes, Geology 17 (1989) 1102–1106.

[2] S.L. De Silva, Geochronology and stratigraphy of the ignimbrites from the 21°30′ to 23°30′ portion of the Central Andes of Northern Chile, J. Volcanol. Geotherm. Res. 37 (1989) 93–131.

[3] S.L. De Silva, P.W. Francis, Volcanoes of the Central Andes, Springer-Verlag, Heidelberg, 1991, 232 pp.

[4] Gonzales-Ferran, Volcanes de Chile, Instituto Geografico Mlitar, Santiago, Chile, 1995, p. 642.

[5] M.E. Pritchard, M. Simons, A satellite geodetic survey of large scale deformation of volcanic centres in the central Andes, Nature 418 (2002) 167–170.

[6] M.E. Pritchard, M. Simons, An InSAR-based survey of volcanic deformation in the central Andes, Geochemistry Geophysics Geosystems 5 (2) (2004) Q02002, doi:10.1029/2003GC000610.

[7] J.A. Naranjo, Sulphur flows at Lastarria volcano in the north Chile, Nature 313 (1985) 778–780.

[8] J.A. Naranjo, Chemistry and petrological evolution of the Lastarria volcanic complex in the north Chilean Andes, Geol. Mag. 129 (1992) 723–740.

[9] R.B. Trumbull, R. Wittenbrink, K. Hahne, R. Emmermann, W. Büsch, H. Gerstenberger, W. Siebel, Evidence for late Miocene to recent contamination of arc andesites by crustal melts in the Chilean Andes (25–26°S) and its geodynamic implications, J. S. Am. Earth Sci. 12 (1999) 135–155.

[10] J.A. Naranjo, P. Cornejo, Hoja Salar de la Isla, N°72, Servicio National de Geologia y Mineria, 1:250000, Santiago, Chile, 1986.

[11] J.A. Naranjo, Geology and evolution of the Lastarria volcanic complex north Chilean Andes, Thesis, Open University, 1986.

[12] J.A. Naranjo, P.W. Francis, High velocity debris avalanche at Lastarria volcano in the north Chilean Andes, Bull. Volcanol. 49 (1987) 509–514.

[13] CNES, Philosophie et mode d'emploi de la chaîne logicielle interférométrique, DIAPASON, Toulouse, France, 1996.

[14] D. Massonnet, K.L. Feigl, Radar interferometry and its application to changes in the Earth's surface, Rev. Geophys. 36 (1998) 441–500.

[15] C. Delacourt, P. Briole, J. Achache, Tropospheric corrections of SAR interferograms with strong topography. Application to Etna, Geophys. Res. Lett. 25 (1998) 2849–2852.

[16] F. Beauducel, P. Briole, J.L. Froger, Volcano wide fringes in ERS synthetic aperture radar interferograms of Etna (1992-1999): deformation or tropospheric effect? J. Geophys. Res. 105 (B7) (2000) 16391–16402.

[17] R. Hanssen, Radar Interferometry Data Interpretation and Data Analysis, Kluwer Academic Publishers, Dordrecht, 2001, 308 pp.

[18] A. Pavez, D. Remy, S. Bonvalot, M. Diament, G. Gabalda, J.L. Froger, P. Julien, D. Legrand, D. Moisset, Insight into ground deformation at lascar volcano (Chile) from SAR interferometry, photogrammetry and GPS data: implication on volcano dynamics and future space monitoring, Remote Sens. Environ. 100 (2006) 307–320.

[19] P. Wadge, W. Webley, I.N. James, R. Bingley, A. Dodson, S. Waugh, T. Veneboer, G. Puglisi, M. Mattia, D. Baker, S.C. Edwards, S.J. Edwards, P.J. Clarke, Atmospheric models, GPS and InSAR measurements of the tropospheric water vapour field over Mount Etna, Geophys. Res. Lett. 29 (2002).

[20] Z. Li, E.J. Fielding, P. Cross, J.P. Muller, Interferometric synthetic aperture radar atmospheric correction: GPS topography-dependent turbulence model, J. Geophys. Res. 111 (B02404) (2006), doi:10.1029/2005JB003711.

[21] Z. Li, J.P. Muller, P. Cross, E.J. Fielding, Interferometric synthetic radar (InSAR) atmospheric correction: GPS, Moderate Resolution Imaging Spectroradiometer (MODIS) and InSAR integration, J. Geophys. Res. 110 (B03410) (2005), doi:10.1029/2004JB003446.

[22] Vuille, Atmospheric circulation over the bolivian Altiplano during dry and wet periods and extreme phases of the southern oscillation, Int. J. Climatol. 19 (1999) 1570–1600.

[23] P. Lundgren, S. Usai, Modeling surface deformation observed with synthetic aperture radar interferometry at Campi Flegrei caldera, J. Geophys. Res. 106 (2001) 19,355–19,366.

[24] C.W. Chen, H.A. Zebker, Phase unwrapping for large SAR interferograms: Statistical segmentation and generalized network models, IEEE Trans. Geosci. Remote Sens. 40 (2002) 1709–1719.

[25] K. Mogi, Relations between the eruptions of various volcanoes and the deformation of the ground surface around them, Bull. Earthq. Res. Inst. Univ. Tokyo 36 (1958) 99–134.

[26] X.-M. Yang, P.M. Davis, Deformation from inflation of a Dipping Finite Prolate Spheroid in an Elastic Half-Space as a model for Volcanic Stressing, J. Geophys. Res. 93 (B5) (1988) 4249–4257.

[27] Y. Fialko, Y. Khazan, M. Simons, Deformation due to a pressurized horizontal circular crack in an elastic half-space, with applications to volcano geodesy, Geophys. J. Int. 146 (2001) 181–190.

[28] V. Cayol, F.H. Cornet, Effects of topography on the interpretation of the deformation field prominent volcanoes—Application to Etna, Geophys. Res. Lett. 25 (1998) 1979–1982.

[29] D.E. Goldberg, Genetic algorithms in Search, Optimisation and Machine Learning, Adison Wesley Publishing company, 1989.

[30] S. Jonsson, Modeling Volcano and Earthquake Deformation from Satellite Radar Interferometric Observation, Standford, 2002.

[31] Y. Fukushima, V. Cayol, P. Durand, Finding realistic dyke models from InSAR data : the February 2000 eruption at Piton de la Fournaise, J. Geophys. Res. 110 (B03206) (2004), doi:10.1029/2004JB003268.

[32] D.F. Mc Tigue, Elastic stress and deformation near a finite spherical magma body: resolution of the point source paradox, J. Geophys. Res. 92 (1987) 12931–12940.

[33] P.T. Delanay, D.F. Mc Tigue, Volume of magma accumulation or withdrawal estimated from surface uplift of subsidence, with application to the 1960 collapse of Kilauea Volcano, Bull. Volcanol. 56 (1994) 7867–7886.
[34] S. Tait, C. Jaupart, S. Vergniolle, Pressure, gas content and eruption periodicity of a shallow crystallizing magma chamber, Earth Planet. Sci. Lett. 92 (1989) 107–123.
[35] Y. Fialko, M. Simons, Y. Khazan, Finite source modelling of magmatic unrest in Socorro, New Mexico and long Valley, California, Geophys. J. Int. 146 (2001) 191–200.
[36] C. Wicks, W. Thatcher, D. Dzurisin, Migration of fluid beneath Yellowstone caldera inferred from satellite radar interferometry, Science 282 (1998) 458–462.
[37] D. Dzurisin, C. Wicks, W. Thatcher, Renewed uplift at the Yellowstone Caldera measured by levelling surveys and satellite radar interferometry, Bull. Volcanol. 61 (1999) 349–355.
[38] L. Christiansen, P. Hsieh, S. Hurwitz, S. Ingebritsen, Numerical Models of Fluid Flow and Crustal Deformation, AGU FALL Meeting, San Francisco, U.S.A., 2005.
[39] P.W. Lipman, The roots of ash flow calderas in Western North America: windows into the tops of Granitic Batholiths, J. Geophys. Res. 89 (10) (1984) 8801–8841.
[40] S. Gudmundsson, J. Marti, E. Turon, Stress fields generating ring faults in volcanoes, Geophys. Res. Lett. 24 (13) (1997) 1559–1562.